Macromolecules
ARTICLE

Macromolecules **2010**, *43*, 8143–8152 **8143**
DOI: 10.1021/ma101033b

Investigation of the Mesostructure of a Mechanically Deformed HDPE by Synchrotron Microtomography

Arnaud Blaise,[†] Christophe Baravian,[†] Stéphane André,*[,†] Jérôme Dillet,[†] Laurent J. Michot,[‡] and Rajmund Mokso[§]

[†]*LEMTA-CNRS 7563-Nancy Université, BP160, 2 avenue de la forêt de Haye, 54504 Vandoeuvre-lès-Nancy, France,* [‡]*LEM CNRS-Nancy Université UMR 7569, 15 avenue du Charmois, BP 40 54501 Vandoeuvre-lès-Nancy, France, and* [§]*Paul Scherrer Institut, SLS, PSI, 5323 Villigen, Switzerland*

Received May 17, 2010; Revised Manuscript Received September 9, 2010

ABSTRACT: Synchrotron X-ray microtomography at submicrometer resolution was used for investigating the evolution with tensile deformation (up to true strains of 1.8) of the microstructure of a semi-crystalline polymer. Different types of data treatment were performed on the obtained image stacks. Combining analysis in real space with 2D FFT transforms, we were able to show that deformed high density polyethylene does not contain any cavities larger than 1 μm, which contradicts the commonly admitted assumption that whitening of HDPE upon necking is associated with a crazing mechanism. In contrast, X-ray tomography reveals that HDPE deformation leads to the development of density contrasts, the spatial repartition of which is strongly anisotropic.

Introduction

Semicrystalline polymers (SCP) are materials with a structure built around the association of amorphous and crystalline domains with a very complex multiscale organization. These materials are attractive for mechanical applications because they realize a good compromise between the lightening of structures and the requirement of performing mechanical properties. In that context, being able to identify robust and consistent behavior laws for such materials is crucial. Indeed, knowing the behavior law of the material is a prerequisite for obtaining reliable simulations using for instance Finite Elements codes. However, at present, such knowledge remains incomplete, mainly due to the fact that the complex relationship between SCPs mechanical behavior and their microstructural reorganization is still far from being clarified.[1] Many factors influence the damage of these materials upon their mechanical solicitation: mechanical loading history, deformation rate, time, temperature (SCP are often used in their vitreous state, which makes them particularly sensitive to temperature effects), manufacturing conditions etc. In addition, after loading, these materials exhibit relaxation phenomena that are rather difficult to quantify. Among SCP's, high density polyethylene has a mechanical behavior that strongly depends on its manufacturing process, which modifies for instance its crystallinity as well as the size and morphology of both the crystals and the spherulites. Figure 1 presents, for a constant strain rate of 0.005 s^{-1}, a typical curve for the evolution of the macroscopic true stress as a function of the true strain. Similar curves are obtained for deformation rates varying between 0.0001 and 0.02 s^{-1}. It must be emphasized that, as shown by Hiss et al.,[2] who studied in detail macroscopic relaxation effects for several SCPs, deformation processes appear to be controlled by strain rather than by stress. Various domains can clearly be identified on such a curve. For very low strains, a limited linear elastic response is observed. The behavior then evolves to viscoelastic before the appearance of a yield point for a strain value close to 0.1 characterized by the development of necking associated with a whitening of the specimen. After the yield point, the mechanical response is characterized by the presence of a pseudoplateau corresponding to a softening of the polymer followed by a plastic or flow regime extending up to a strain value around 1.1. Up to the strain value of about 0.5, the mechanical behavior remains fully reversible.[2] The material then starts hardening. Referring to the recent paper by Haward,[3] the point where the differential nominal stress becomes positive (in terms of extension ratio), sometimes called the second Considere condition, is obtained for a value of 1.1. It corresponds to the stabilization necking condition and is considered as the transition between the visco-plastic flow regime and the hyper-elastic or strain-hardening one.

The microstructural transformations associated with these various ranges of deformation have been studied by numerous authors[4−21] who try to identify the pertinent observation scale and main mechanisms responsible for the global macroscopic behavior. Important results have been obtained for the last 4 decades, thanks to the coupling between precise microstructural investigation techniques and controlled macroscopic true strain paths applied to the samples.[22] Despite these efforts, a complete scenario describing the dynamical processes leading to topological rearrangements of the structure is not available in the case of crystalline polymers, where various classes of phenomena can occur simultaneously at different scales.

i. Some phenomena are located in the crystalline phase. Numerous studies have indeed identified various mechanisms occurring upon tensile/compressive deformation such as the role of slip systems, twinning, stress-induced (martensitic) transformation[4−7] and fragmentation (melting) and recrystallization events.[8]
ii. Some phenomena are related to the interactions between the amorphous phase and the crystals (interlamellar evolutions, role of the tie molecules, molecular motions at segmental scale...).[9−12]
iii. Cavitation or crazing phenomena have been suggested by Kramer[13] and many others.[14−18] Voiding appears

*Corresponding author.

Published on Web 09/17/2010

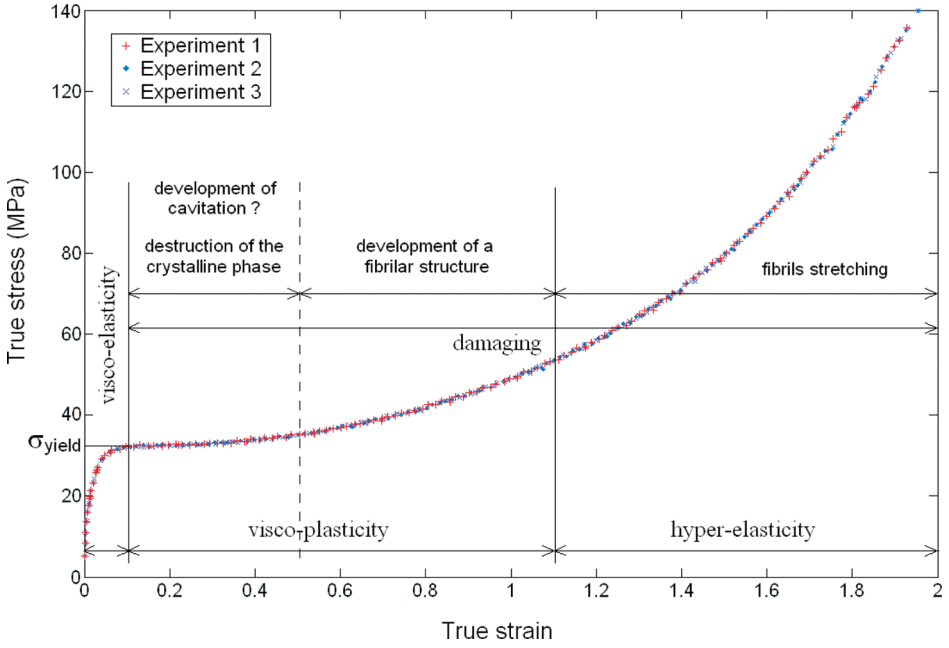

Figure 1. True stress−true strain curve obtained on three HDPE specimens under a tensile test (constant strain rate of $\dot{\varepsilon}_{11} = 0.005\ s^{-1}$).

to proceed by nucleation that then propagates in terms of volume fraction, size, morphological alteration. It can be considered as an adjustment or delocalization[1] mechanism that provides some degrees of freedom to a constrained microstructure.

iv. At the mesoscopic scale, the deformation of spherulites can to some extent explain the macroscopic behavior of polymer. This is particularly the case of the change from a spherulitic organization to a fibrillar structure observed at high strains.[19−21]

Obviously all these phenomena can occur simultaneously or in a delayed manner and are strongly interdependent. The associated scientific challenge is then to establish a scenario of the whole process of morphological transformation of the initial structure. The present paper focuses on processes occurring at scales iii and iv. In that range, whitening and softening above the yield point are classically interpreted as resulting from the development of microcavities inside the material. Whitening is then interpreted as resulting from the scattering from microvoids a few tens of nanometers in size.[18] Using small angle X-ray scattering (SAXS), Butler et al.[5] have, for instance, shown that samples whiten when both the martensitic transformation and voids formation occur. According to their results, the voids first undergo an extension perpendicularly to the tensile axis. Such a scheme of cavity development has been retained by numerous authors,[23] who consider that void development is influenced by the "balance" between the crystalline and amorphous phase, with the hydrostatic pressure or stress triaxiality as a governing factor.[11,17] Indeed, increasing mobility of the amorphous phase inhibits the formation and growth of cavities. This occurs for instance at high-temperature and/or for reduced strain rates. In contrast, highly crystalline materials exhibit intense cavitation as, in such conditions, the amorphous phase is more constrained. Pawlak[16] links the presence of voids in deformed polymers to the elastic limit of the crystalline phase. Also the size of the spherulite has a pronounced impact on cavitation. The cavitation process is also often invoked to explain important volume expansion in the plastic domain.[17]

For strain values larger than 0.5−0.6, i.e., at the onset of irreversibility corresponding to chain disentanglement,[2,6] the structure clearly becomes anisotropic, as revealed by SAXS[7,8] and multiple light scattering experiments.[24,25] In the framework of voids development, this corresponds to the orientation of voids along the tensile axis, separating fibrillar structures. A gradual strain hardening is then observed when this network is stretched up to large strains. The microstructure at high deformations then consists of highly oriented microfibrils (stacks of lamellae) organized into fibril bundles (fibers) with diameters of a few tens of nanometers and lengths of a few hundreds of nanometers.[20,26,27]

Although numerous studies devoted to the mechanical behavior of SCPs have been performed, some aspects related to the development of anisotropic structures clearly deserve further attention. For instance synchrotron-based SAXS experiments[28] do not univocally establish which phases (dense crystalline objects, less dense amorphous regions, microfibrils, voids) are responsible for the scattered intensity. In such a context, the use of non intrusive 3D techniques with minimal sample preparation could provide new insight into the mesostructural aspects of damaging in SCPs. In particular, synchrotron-based X-ray microtomography appears as a very well adapted technique for studying the evolution of the morphological features of a HDPE polymer at different deformation levels. The present paper then focuses on experiments carried out by X-ray microtomography with a pixel size of 0.38 μm on a series of HDPE polymer samples subjected to various strains beforehand. We will show that such an experimental approach provides very relevant information about structure anisotropy, while raising some questions about the commonly accepted model of whitening related to voids formation.

Materials and Methods

Preparation of the Predeformed Samples. The material tested in this work is a HDPE (high density polyethylene, grade "500 Natural", molecular weight 500 000 g/mol, density 0.95 g/cm^3) produced by Röchling Engineering Plastics KG. The specimens were manufactured by extrusion and supplied as sheets. Differential scanning calorimetry yielded a crystallinity index of about 68 wt % for the specimen. Bone-shaped samples were cut from a 6 mm thick sheet of polymer and machined in order to get a narrower central part of square section 6 mm by 6 mm.

All mechanical tests were performed on a servo-hydraulic MTS 810 load frame with Flextest SE electronic controller. A video-extensometer similar to those initially developed by G'sell et al.[22] (VidéoTraction system developed by Apollor Union, France) provides the elastoviscoplastic response of polymers under uniaxial tension. Local measurements of true strains are performed at the center of the sample i.e. at the maximum strain location (where necking takes place). The measurement of the corresponding force enables plotting the axial true stress−true strain curve for the sample. As the system controls the servo-valve of the machine in real time (through a feedback loop), any desired input path of true strain ε_{11} can be imposed on the specimen. Fourteen samples of HDPE were stretched until various predefined maximal true strains ε_T (from $\varepsilon_T = 0$ up to $\varepsilon_T = 1.80$). All tensile tests were performed in the same way. First, a tensile phase at constant strain rate $\dot{\varepsilon}_{11} = 5 \times 10^{-3}$ s^{-1} was carried out. The strain rate was then reversed until the true stress reaches a zero value. Lastly, the system was maintained at zero stress for about 20 min allowing for relaxation, before the sample was removed from the machine. The final strain measured at the end of this recovery stage is recorded and denoted by ε_F in Table 1. Figure 2a presents a schematic protocol of the realized tests whereas parts b and c of Figure 2 display the temporal evolutions of the true strain and true stress for different tensile elongations ε_T. Using such a protocol, relaxation effects following the tensile test are significantly reduced. Still, as microtomography experiments were carried out about 1 month after the tensile tests, relaxation proceeds further and this new strain state ε_M has been roughly estimated after the tomographic experiments thanks to the black markers (used for videomonitoring of the strain during the measurements) still printed on the surface of highly deformed samples. Table 1 sums up the values of the various strains. The difference between strains at the end of the tensile experiments (ε_F) and the relaxed ones (ε_M) is about 0.3 for highly stretched samples and decreases with decreasing strain.

Table 1. Values of the True Strains ε_T, ε_F, and ε_M for Each Deformed Sample

sample	ε_T	ε_F	ε_M
1	0	0	0
2	0.12	0.03	0.02
3	0.20	0.07	0.06
4	0.30	0.12	0.10
5	0.40	0.19	0.15
6	0.50	0.27	0.22
7	0.60	0.35	0.28
8	0.70	0.44	0.35
9	0.90	0.64	0.51
10	1.10	0.84	0.67
11	1.30	1.06	0.85
12	1.50	1.29	1.03
13	1.65	1.47	1.18
14	1.80	1.65	1.32

In the next sections, the analysis of the tomographic data is based on the different "after-one-month" strain states ε_M. Still the discussion and interpretations of the results are based on the scenario summarized on Figure 1 that uses the true dynamic strain measurements ε_T. Table 1 can then be used for establishing appropriate correspondences.

Prior to the tomography experiments, the samples were cut, approximately 4 mm above the central zone (necked area) where the measurements of true strain were carried out. They were then turn-machined at very low rotation speed (to limit heating) until a circular section approximately 3 mm in diameter (Figure 3) was obtained.

X-ray Microtomography Experimental System. Experiments were carried out at the TOMCAT beamline of the Swiss Light Source (Villigen, Switzerland). The X-ray energy was adjusted to 10 keV by means of a double crystal multilayer monochromator (DCMM) located at approximately 7 m from the X-rays source, which is a superbending magnet. The broadband radiation exiting the monochromator has an anguar divergence of 2 mrad by 0.6 mrad with a stream of 5×10^{12} (photons/s)/mm^2. The tomographic stage is set up at 25 m downstream from the X-ray source, where the dimensions of the beam are about 40 mm by 9 mm, but only a fraction of this is used in the current study. In order to condition the beam, four filters are arranged at the head of the station. The sample is placed vertically on a platform that ensures a translation in each direction of space (accuracy: 1 μm). The rotation speed of the platform can reach 360° per second. Axis z is the vertical axis corresponding to the longitudinal tensile axis. The sample in Figure 3 was adjusted in height z so that the beam passes in the exact center of the necked area with persistent strong white color.

After interacting with the sample, X-rays are collected on a CCD detector (2048 × 2048 pixels, 14-bit intensity) mounted on an optical microscope coupled to a 20 μm thin scintillator screen. The microscope allows to change the magnification from 1.25× up to 20×. In the present work, the 20× objective was used to reach the highest resolution (pixel size of 0.38 μm × 0.38 μm), which results in a spatial resolution of slightly below 1 μm and allows hence to clearly distinguish features in the object larger than 1 μm. The field of view in this configuration is

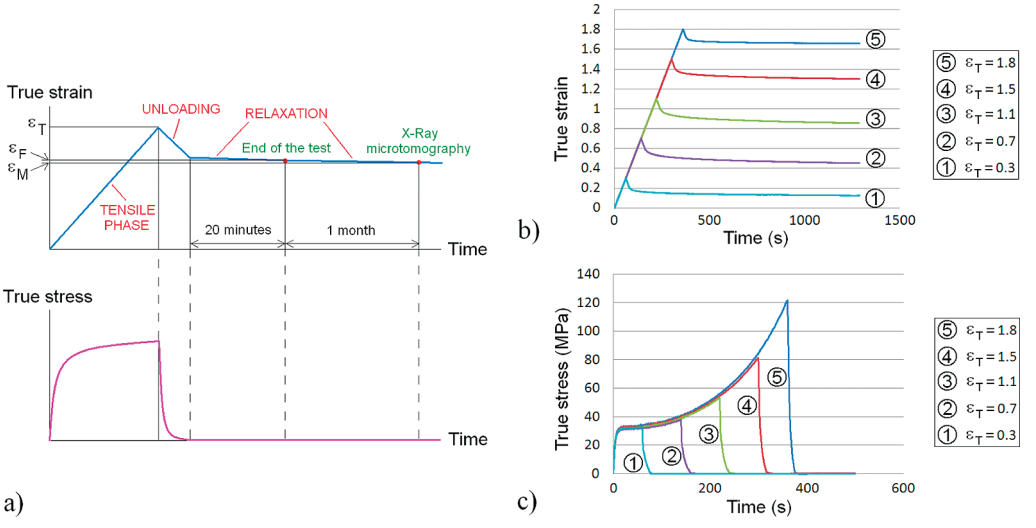

Figure 2. (a) Schematic description of the tests. (b) Several experiments showing true strain in function of time. (c) True stress as a function of time of the same experiments.

0.75 mm as compared to the typical sample sizes of 4−6 mm. In a computerized tomography (CT) experiment (Figure 4), radioscopic projection images are recorded for a well-defined set of angular positions of the sample (1501 projections for a total angular sector of 180°). Using phase contrast technique and adapted mathematical algorithms developed at SLS, quantitative three-dimensional images of the X-ray absorption coefficient can then be obtained. A complete reconstructed volume has a size of 2048 × 2048 × 2048 pixels with16-bit depth. In the present case, we systematically worked on smaller volumes of 501 × 501 × 501 pixels (extracted from the central part of the main stack, 8-bit intensity depth), which minimizes calculation times while still allowing a proper analysis of the evolution of the mesostructure. Image analysis was performed using two different procedures. The raw images were first analyzed in real intensity. They were also processed through 2D process fast Fourier transforms (FFT) in the three directions x, y, z in order to study intensity maps in the reciprocal space.

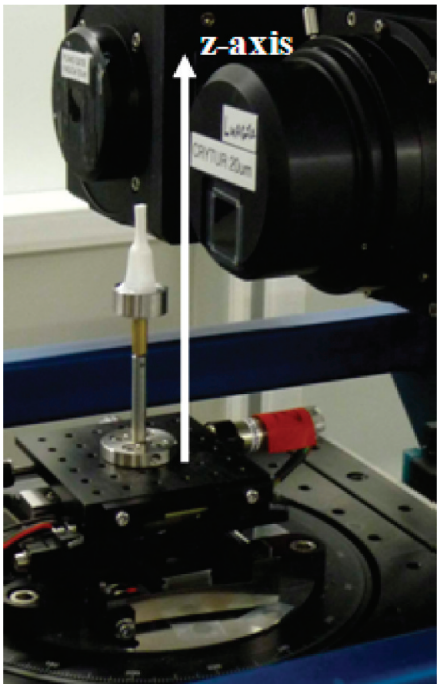

Figure 3. Photograph of a sample in the tomography setup.

Image Analysis

Analysis in Real Intensity. In this section, the distribution of the gray levels of the images is studied as a function of the final corrected true strain ε_M of the stretched samples. Figure 5 provides an example of the raw 3D objects, obtained after reconstruction. Figure 5a shows the original reconstructed image of 2048 × 2048 pixels corresponding to the upper face (perpendicular to the z-axis). As described above, the field of view is considerably smaller than the sample size, therefore so-called local tomography mode has been employed. This is depicted in Figure 5a where the signal extends throughout the complete square of 2048 × 2048 pixels, while only the inner part of the visible ring contains the required information for the tomographic reconstruction. In other words the inner part of the ring is the useful region of the reconstruction. As previously mentioned, data analysis was performed on 3D cubes, 500 voxels in size, extracted internally in the middle of the original cube (Figure 5, parts b and c). Figures 5b and 5c present the reconstructed volumes corresponding to a nondeformed original HDPE sample and to a highly stretched structure ($\varepsilon_M = 1.32$), respectively. A visual comparison between these two images reveals significant changes that need to be further analyzed.

First, the gray level distribution of each image of the stack (taken in each direction x, y, and z) has been determined. Then, these 3 × 500 distributions have been averaged resulting in 3 averaged gray level distributions (one for each direction). The gray level distribution (between 0 and 255) displays a Gaussian shape, whatever the considered true strain and analyzed direction (Figure 6). With increasing strain, both the intensity (insert in Figure 6) and width of the Gaussian distribution evolve until they reach constant values for a true strain ε_M of 0.51. The slight differences between the two curves $P_{g_M}(\varepsilon_F)$ and $P_{g_M}(\varepsilon_M)$ illustrates the negligible

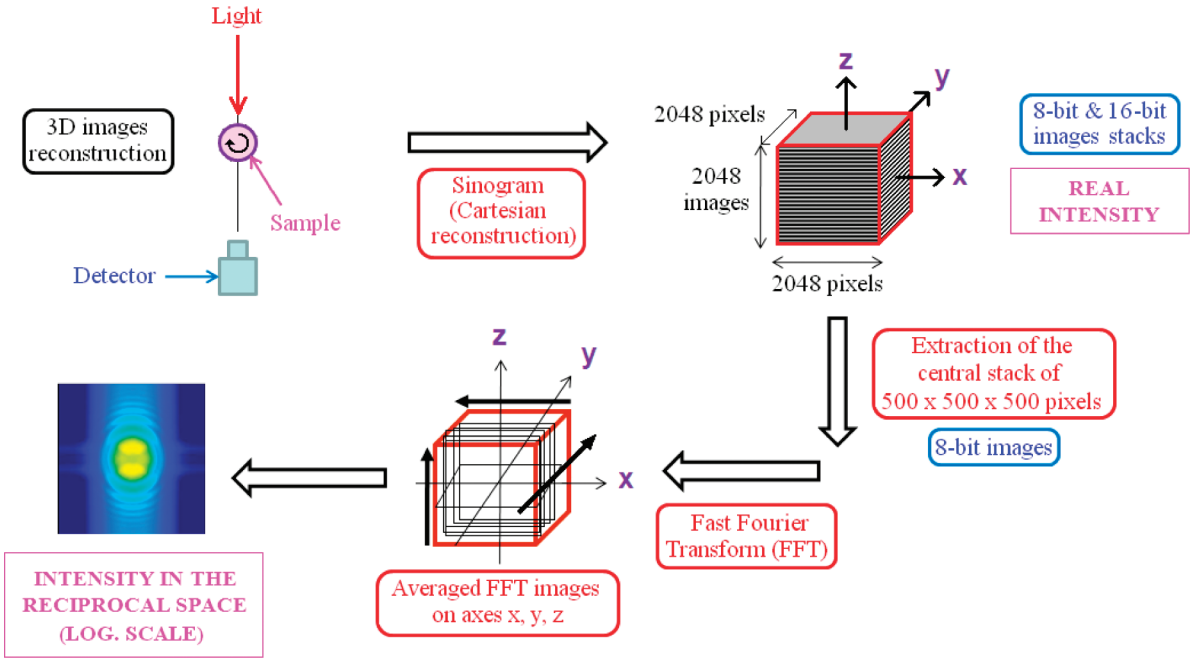

Figure 4. Schematic representation of the treatment applied to tomography images.

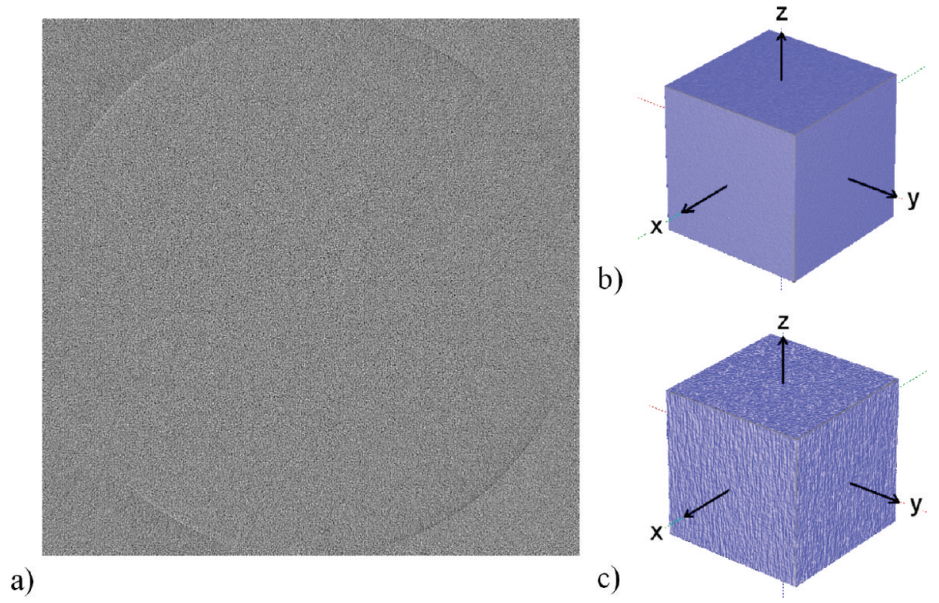

Figure 5. Examples of 3D objects obtained from the X-ray tomography analysis: (a) Original slice of 2048 × 2048 pixels (upper face); (b and c) extracted volumes of 500 voxels at $\varepsilon_M = 0$ (sample 1) and $\varepsilon_M = 1.32$ (sample 14) deformation, respectively.

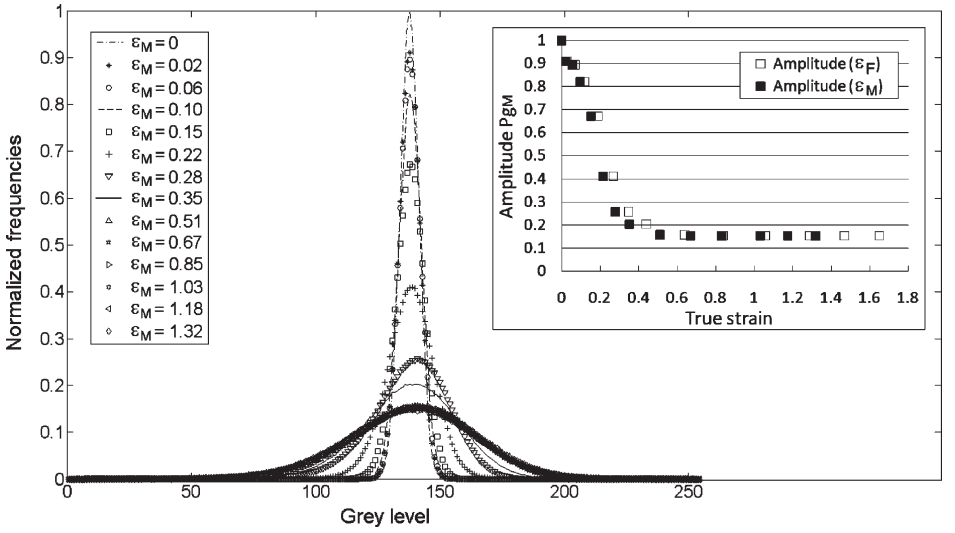

Figure 6. Images gray level distributions as a function of true strain ε_M. Insert: normalized amplitude of the Gaussian curves versus ε_F and ε_M (shifted).

effect of strain recovery with time following the zero-stress holding period. The Gaussians curves in Figure 6 have all been normalized by multiplication by the std of the initial distribution ($\varepsilon_M = 0$ − undeformed sample). The curve reported in the inset of Figure 6 shows the evolution of the normalized maximum peak of the Gaussians. (It also corresponds to the ratio σ_1/σ_i of the s.t.d σ_1 of the initial distribution to the s.t.d σ_i of the distribution corresponding to the ith experimental data point). It will be referred to as Pg_M in the following, where g_M stands for median gray level intensity. Peak intensities are maximal for the smallest strains until ε_M equals to 0.06, i.e., for samples before the yield point (Figure 1). A significant drop in peak intensity can be observed for higher strain values up to ε_M of 0.51, i.e., at the end of the plastic regime in the $\sigma - \varepsilon$ curve (Figure 1). The Gaussian then remains constant for higher strain values.

As the gray levels are linked to X-rays absorption contrasts, their evolution reveals some features of evolution of the microstructure with deformation. In the nondeformed state, the narrow histogram indicates the presence of homogeneously distributed objects. The widening of the histograms with constant median suggests that upon deformation, the absorption properties of the initial structures start being discriminated. This is visually evidenced in Figure 5c that reveals the presence of oriented structures with contrasting X-ray absorption. Similar features were observed on AFM images obtained on HDPE.[27] It must be pointed out that such structures can explain the whitening of the sample occurring upon deformation in the zone where a marked widening of the histograms is observed. The fact that the median gray level intensity g_M remains the same in the course of the deformation path could indicate that the global volume fraction of both the crystalline and amorphous phase remain the same. This is not in agreement with a scenario implying melting and recrystallization stages.

The results of Figure 6 (insert) are in perfect agreement with those obtained using a light scattering technique.[24,25] This technique allows the measurement of the characteristic transport length l_{Tr} of turbid materials. It is then a way to precisely quantify the whitening of HDPE samples under drawing.

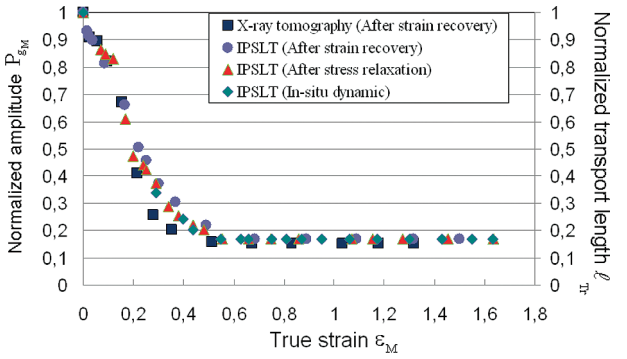

Figure 7. Comparison between X-ray tomography experiments and light scattering experiments (IPSLT technique).

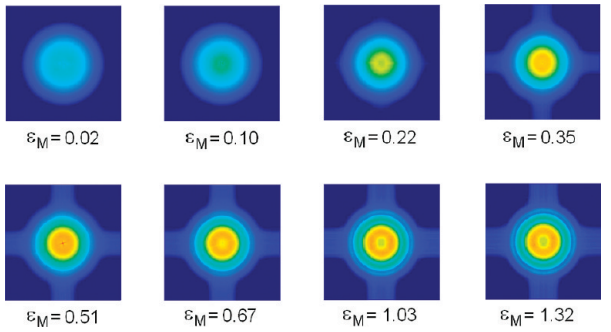

Figure 8. 2D-FFT patterns obtained for the images taken perpendicularly to the longitudinal tensile *z*-axis.

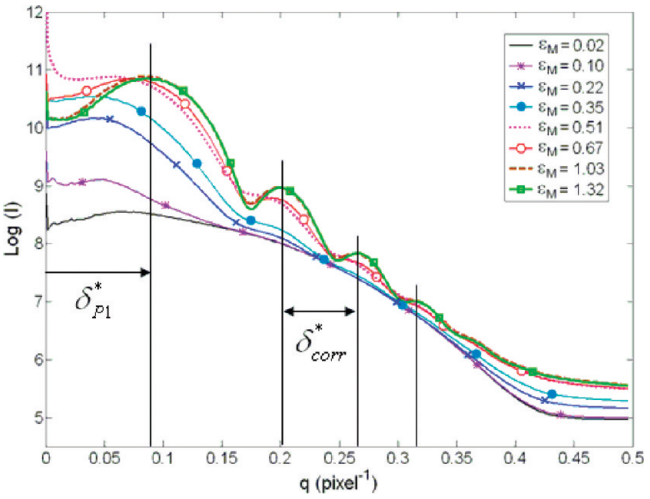

Figure 9. Intensity (in log scale) versus reciprocal space distance plotted for different values of ε_M of the HDPE samples (resulting from isotropic 2D-FFT patterns of Figure 8).

This laboratory technique is fast enough to allow for real-time in situ characterization of specimens.[24] Figure 7 plots the tomographic data Pg_M (ε_M) along with the data obtained by incoherent polarized steady-light transport (IPSLT technique) during stretching (curve "in situ"), after stress relaxation (curve "relaxed"), and after unloading until zero-stress (curve "strain recovery"). This latter then corresponds to the conditions under which tomographic experiments were carried out (curve "X-ray tomography" from Figure 6). All these curves match perfectly which (i) proves that it is the strain level achieved during initial stretching that determines the whitening level of the sample (no obvious effect due to relaxation or recovery) and (ii) proves that the whitening evolution characterized by the IPSLT technique follows the exact same path as the one given by tomography experiments (same submicrometer probing scale). In the fibrillar state especially, even if strong recovery is observed during the one-month delay (inset of Figure 6) for very high strains, the maximum intensity of the whitening effect was already definitely obtained.

FFT Processing. FFT processing of the images was carried out in order to obtain quantitative information about the average size of the objects exhibiting an absorption contrast with respect to the polymer matrix and the anisotropy developed by the structure upon stretching. Reconstructed 2D images obtained on each observation axis were then processed using the conventional 2D FFT routine of Matlab and averaged.

Analysis of Correlation Features

For determining the average size of the objects, images obtained perpendicularly to the *z*-axis were used. Figure 8 displays some of the intensity maps obtained in the $x-y$ plane in the reciprocal space for various strains. All patterns are isotropic and display clear modulations for $\varepsilon_M > 0.06$. Figure 9 shows the corresponding evolution of the intensity profile as a function of spatial frequency q (in pixel^{-1}). For deformations higher than 0.1, clearly resolved peaks are observed, which can be assigned to the presence of short-range correlations in the structure. The peaks sharpen with increasing strain (from $\varepsilon_M = 0.51$) and remain nearly unchanged for higher strain values. Two families of peaks are observed. Higher order modulations (for $q \geq 0.2$ px^{-1}) are rational with a period of around $\delta^*_{corr} = 0.06$ px^{-1}, and their position on the q axis is independent of strain. Another peak δ^*_{P1} is clearly visible at low q values and its position evolves with increasing strain. Converting δ^*_{corr} in the reciprocal space distance $\delta_{corr} = \delta^*_{corr} \times 0.38^{-1}px^{-1}\cdot\mu$m^{-1} brings a typical correlation length $l_{corr} = 1/\delta_{corr}$ of about 6−7 μm For strains $\varepsilon_M \leq 0.1$, the first peak location can not be assessed precisely and no data is considered available in this range. Results obtained by FFT processing suggest that damage in the early deformation stages (but above the yield point), leads to the apparition in the structure of differentiated objects with contrasting density. Such a vision concurs with previously obtained results for HDPE or other SCP's[2,7,15,16,19,20] that clearly establish that, under strain, the uniform initial biphasic structure organized in spherulites evolves through destruction of the spherulites, ruptures and phase transformation in the crystalline aggregates. At the end, it produces a fibrillar structure associated macroscopically with necking.

In order to better assess the quantitative FT treatment, simulations were performed assuming a random distribution of perfect disks of constant diameter D with various volume fractions (Figure 10a). Figure 10b displays the intensity profile obtained from the FT of the thus generated images. It exhibits highly resolved peaks, very similar to those obtained experimentally at the highest deformed state ($\varepsilon_M = 1.32$) and at the same position. The peaks positions are independent of the volume fraction of the disks and depend only on the value chosen for the disk diameter D. For a value of 7 μm (Figure 10a, right), the simulation results are close to the experimental FFT profiles (Figure 10b). All peaks on the simulated curves are obtained on the experimental curve except for the second one. The experimental peaks are however significantly broader than the simulated ones. This is due to polydispersity effects. Indeed, when polydispersity is introduced in the simulation (not shown), the peaks at low q values are broader and the high q peaks tend to fade. No explanation can be provided at present for the absence of the second peak at $\delta^*_{extra} = 0.14$ in the experimental results (though a shoulder is visible). Simulations made using more complicated objects such

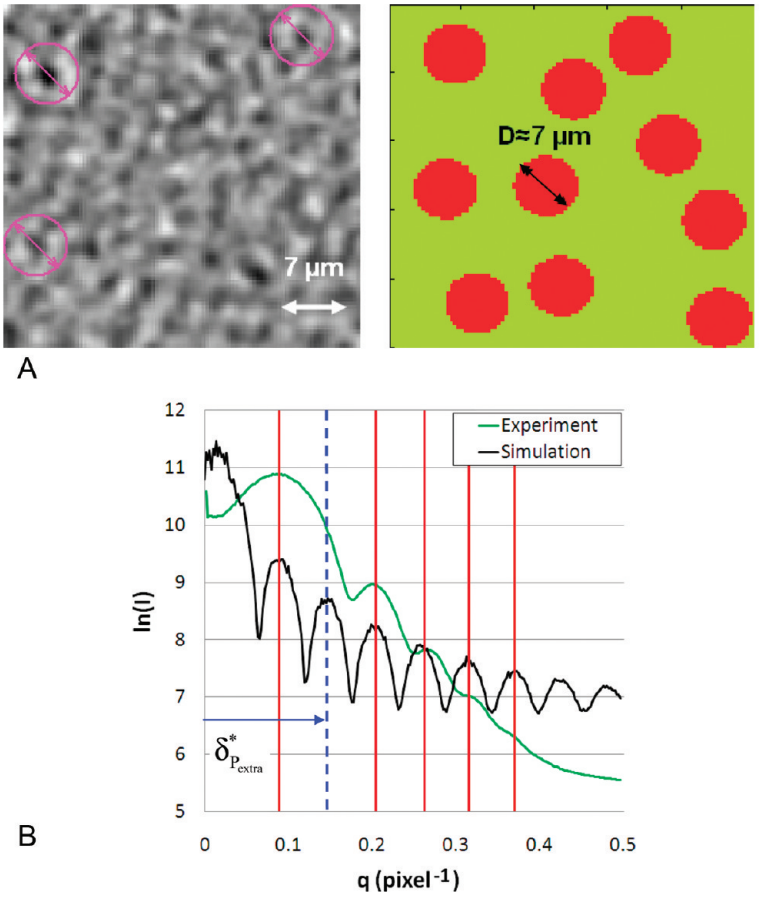

Figure 10. (a) Tomographic image obtained for $\varepsilon_M = 1.32$ perpendicularly to the tensile z-axis and idealized image used for the simulation of FFT profiles of part b. (b) Fourier intensity (in log scale) versus reciprocal space distance plotted for both the experimental tomographic images (curve of Figure 9, $\varepsilon_M = 1.32$) and a simulation based on disk-shaped objects (part a).

as core−shell bodies clearly lead to the appearance of new peaks. It is however rather tricky (and this is not the object of the present section) to pretend identifying the topological structure by this trial and error process as no univocal solution can be derived. Still, the performed simulation strongly suggests that the vision of highly deformed HDPE as formed with relatively regular objects with higher density than that of the matrix captures most of the features of the tomographic images.

As anisotropic features are clearly observed for highly deformed samples (Figure 5c), it is relevant to apply the Fourier treatment in the other directions to obtain information about the shape of the denser objects. Further information on the shape of the denser objects can be obtained by tomography by applying a similar Fourier treatment to images (x−z) and (y−z), taken in the longitudinal-section plane. Figure 11 then presents 2D intensity patterns (x−z plane) obtained in the reciprocal space as a function of ε_M (similar results are obtained for y−z images). In addition to strong anisotropic features developing along both the tensile z-axis (horizontal axis of the patterns) and the transverse directions x and y, that will be discussed in the following sections, intensity modulations are clearly observed.

Parts a and b of Figure 12 present the evolution of the intensity as a function of inverse distance in the horizontal and vertical directions, respectively. Along the horizontal direction, the peaks sharpen continuously with increasing true strain and the obtained profiles are similar to those of Figure 9.

Along the vertical direction (Figure 12b), peaks are located at the same positions. They are however more numerous and more intense with a maximum in intensity for a true strain of $\varepsilon_M = 0.51$. This latter observations suggest that dense objects develop

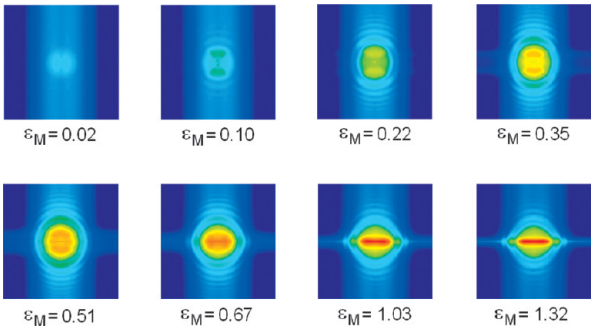

Figure 11. 2D-FFT patterns obtained for the images taken sideways in the sole x-axis from the reconstructed volume as a function of ε_M.

with the same spatial periodicity in both directions. This could correspond to objects evolving from a spherical shape to a z-oriented cylindrical shape with increasing strain

Image Anisotropy Analysis

In the patterns of Figure 11, a first anisotropy develops in the vertical direction for low strains ($\varepsilon_M \leq 0.35$), *i.e., in the plane perpendicular to the tensile axis*. For an ε_M value of 0.51, the pattern is nearly isotropic, whereas for higher values, an horizontal anisotropy, i.e. along the tensile z-axis, starts appearing. This latter anisotropy seems to increase with increasing strain.

Figure 13 displays the angular variation of intensity at a radial distance corresponding to the first peak of the FFT for various final strains ε_M. Angles at 0° and 180° correspond to the tensile z-axis. The anisotropy observed on the images is confirmed from

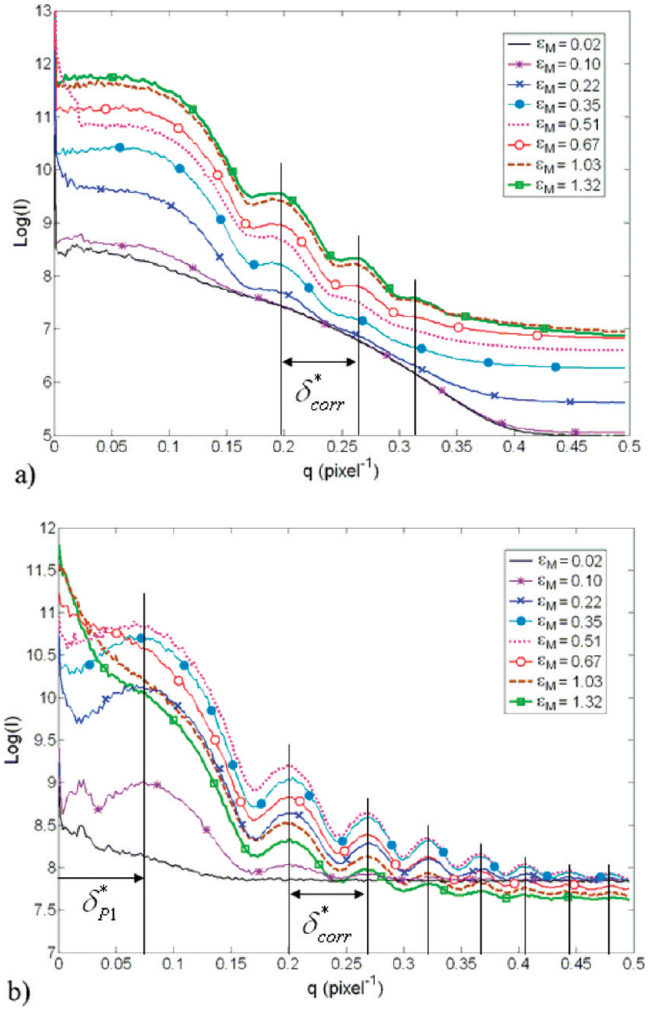

Figure 12. Intensity (in log scale) versus reciprocal space distance plotted for different values of ε_M of the HDPE samples (resulting from anisotropic 2D-FFT patterns of Figure 11). (a) Horizontal direction. (b) Vertical direction .

these plots that reveal a clear evolution of the anisotropy with strain, and especially an inversion of the direction of anisotropy that can be observed between the patterns at $\varepsilon_M = 0.35$ and $\varepsilon_M = 0.67$. In order to derive quantitative information from these curves an anisotropy index was defined as:

$$A(\varepsilon_M) = \frac{I_H(\varepsilon_M) - I_V(\varepsilon_M)}{I_V(\varepsilon_M) + I_H(\varepsilon_M)}$$

where I_V and I_H are the linear intensities calculated from the logarithmic intensities measured for the vertical and horizontal directions of the FFT images (Figure 11) as shown in Figure 13. This index definition comes from the theory of light transport by scattering. It is connected to the special behavior, in given directions, of the phase function, which allows calculating the scattering component in the radiative transfer equation. It presents the advantage of evolving between -1 (full transverse anisotropy) to $+1$ (full longitudinal anisotropy). Another index can be used, that is thoroughly used to characterize anisotropy of images (media) in diffraction studies.[29] It is Hermans orientation factor defined as

$$f = \frac{3\langle\cos^2\phi\rangle - 1}{2}$$

where $\langle\cos^2\phi\rangle$ is the mean cosine defined by

$$\langle\cos^2\phi\rangle = \frac{\int_0^\pi I(\phi)\cos^2\phi\sin\phi\,d\phi}{\int_0^\pi I(\phi)\sin\phi\,d\phi}$$

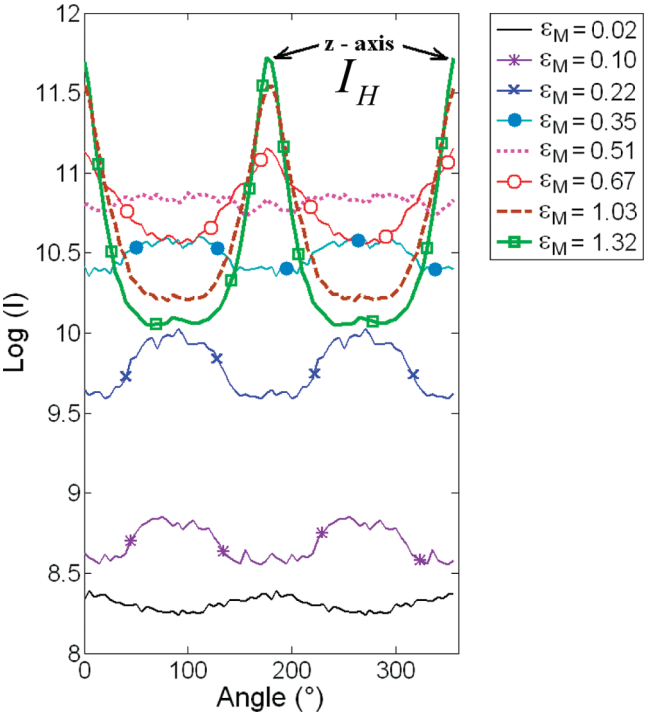

Figure 13. Angular intensity variation taken at the first peak position δ_P* of Figure 12b. The arrows indicate the horizontal direction of the FFT images which corresponds to the tensile axis in the real space.

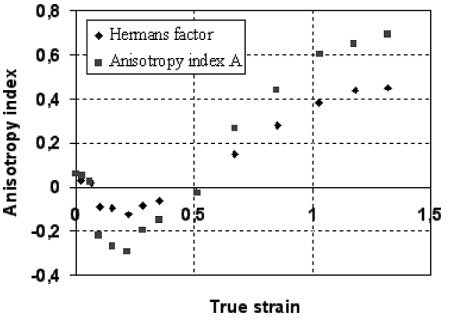

Figure 14. Anisotropy index A and Hermans factor as a function of ε_M.

where ϕ is the averaged value of the square of the cosine of the angle ϕ between the z-axis of the sample and the objects orientation principal axis (angle expressing the dependence of I on Figure 13). It varies from $-1/2$ to $+1$.

Figure 14 presents the evolution of both anisotropy indexes as a function of ε_M. They are not exactly zero in the undeformed state because of the anisotropy induced in the direction of the extrusion process (tensile specimen longitudinal axis). Anisotropy index A decreases for $0.06 \leq \varepsilon_M \leq 0.22$ and exhibits a minimum for $\varepsilon_M = 0.22$, i.e., the strain that is generally considered to correspond to the onset and development of the fibrillar structure from the initial spherulite organization. Then, this index reverses to cross the zero level for a value of $\varepsilon_M = 0.51$. The strong increase observed at high strain can be associated with the fibrillation of the deformed polymer. Both indexes naturally exhibit the same trend.

Discussion

The evolutions of Pg_M and A with ε_M are plotted together in Figure 15. Both quantities do not evolve at very short strains, before the yield point. The tomography patterns remain isotropic in this range until point A_0^1. Above the yield point severe

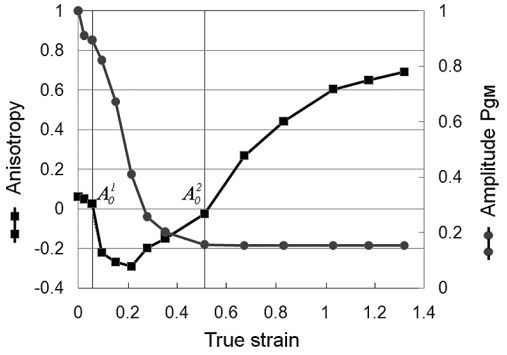

Figure 15. Anisotropy index A and amplitude peak Pg_M deduced from gray-level images, plotted as a function of ε_M.

transformations occur in the material as evidenced macroscopically by necking and whitening. Two stages can be clearly defined about the strain $\varepsilon_M = 0.51$ which plays a key role in the observations. In a first phase, $\varepsilon_M \leq 0.51$, Pg_M significantly decreases whereas the measured anisotropy develops first perpendicularly to the tensile z-axis before reversing parallel to it. For higher strain values $\varepsilon_M \geq 0.51$, Pg_M remains constant, which means that the structure of the objects (the fibrils in that stage) is now established. The anisotropy index strongly increases from 0 (point A_0^2) to 0.7. Such a behavior suggests that a strain value ε_M of around 0.5 corresponds to the onset of the fibrillation process (it refers to a true strain of $\varepsilon_T = 0.9$ during a live tensile test, see Figure 1). Above that point, the fibrils first orientate along the tensile z-axis. This mechanism is less and less dominant (the slope of the anisotropy signal decreases at very large strains). The fibrils are more and more defined in a cross section from an elliptic to a disk-shape geometry, which decreases the dispersion around the average "diameter". This probably explains the growing resolution and reinforcement of the peaks observed in the FFT profiles (Figures 9 and 12). Second, the fibrils undergo a macroscopic extension.

In contrast, the origin of the transverse anisotropy observed for low strains remains unclear at present. It was already observed in the backscattered intensity images obtained by incoherent light transport[30] and in SAXS experiments.[16] In that latter case, this initial anisotropy was interpreted as resulting from the development of crazes, around 40 nm in size elongated perpendicularly to the strain direction. However, no definite answer regarding this question can be provided, yet. It must be pointed out that the tomography experiments described in the present paper do not evidence any formation of cavities in the material upon straining, although such an explanation is often proposed in the literature,[6,7,14,16] to account for the whitening of the HDPE samples. The absence of any cavitation phenomenon (even though it is not responsible of the whitening) may be explained by the initial structure of the material that does not present any spherulitic structure as shown in Figure 16. Only a few very small Maltese crosses can be detected on the original images produced by the microscope.

It must be emphasized that, in view of the sensitivity of synchrotron-based tomography, the presence of cavities larger than 1 μm^3 (corresponding to 9 voxels) would have been easy to detect. Such a statement is illustrated in Figure 17 that presents the reconstruction of a sample where a large cavity with very strong absorption contrast likely due to the presence of a defect can be observed. Moreover due to the presence of phase contrast information simultaneously present in every image acquired with partially coherent X-rays at synchrotron sources, the presence of submicrometric cavities is detectable. It can then be safely stated that the whitening of the HDPE samples studied in the present paper cannot be assigned to the formation of cavities

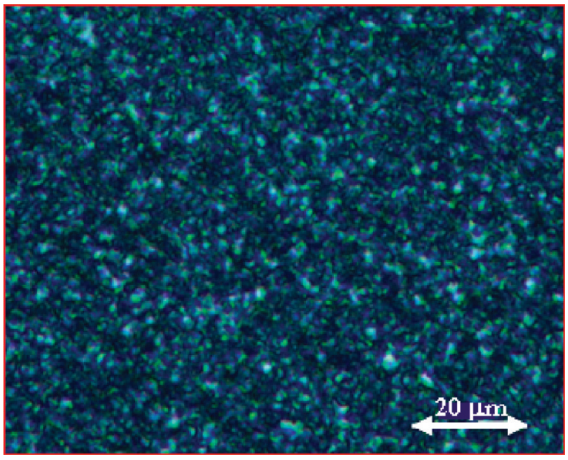

Figure 16. Structure of unstretched HDPE under cross-polarized microscope (absence of any spherulitic structure).

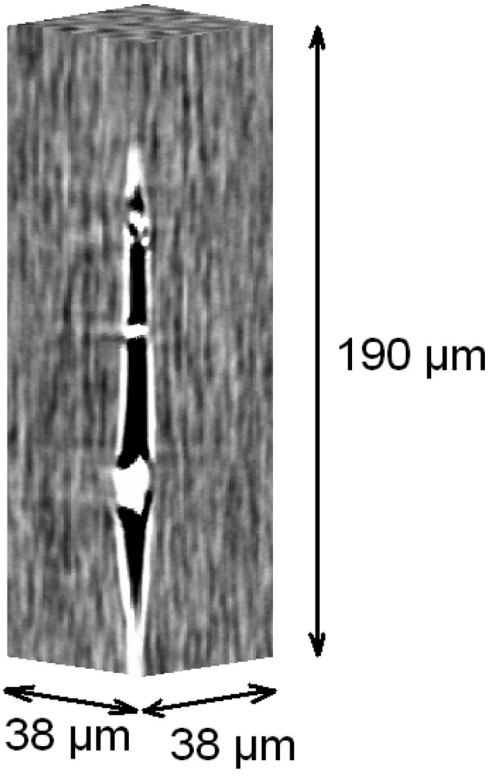

Figure 17. 3D microtomography showing a large very rare hole in a sample – deformation of $\varepsilon_M = 1.32$ (manufacturing defect or local rending?).

larger than some hundred nanometers in size. Still, the existence of much smaller holes in the samples cannot be ruled out. Indeed, the existence of voids smaller than 40 nm was inferred from SAXS measurements on deformed samples.[16] However, as shown by preliminary polarized light scattering experiments,[30] this cannot explain sample whitening. Consequently, whitening must be assigned to scattering by a medium formed with objects having an electronic density contrast compatible with the refractive index ratio responsible of the light scattering and probably due to the apparition of a second crystalline structure as revealed by recent in situ WAXS/SAXS studies. This may argue with a microscopic organization of the deformed structure as paracrystalline macrolattices as initially suggested by Hosemann[31] and also putted forward by other authors.[29]

Conclusion

Post-mortem X-ray tomography experiments have been performed on various predeformed samples of a semicrystalline polymer (HDPE). Synchrotron-based microtomography clearly appears as a very adapted tool for studying the morphological evolution of semicrystalline polymers subjected to strain at the micrometric scale. Analysis in both the real and reciprocal space allows deriving a structural evolution related to the formation of fibrils with increasing anisotropy and reduced section, the various evolutions being linked to the features of the stress/strain curves. Such experiments also show that the whitening of the samples occurring after the yield point cannot be assigned to the formation of cavities larger than 1 μm^3 inside the sample. As a consequence, this tomographic study tends to prove that a mesostructural organization built around crystalline and amorphous objects of micrometer size (paracrystalline lattice) is likely more able to model the macroscopic behavior. It would be particularly relevant in that context to collate tomography experiments with experiments probing the same spatial range such as incoherent polarized steady-light transport. Obviously characterization at the micrometric scale should be combined with experiments allowing to analyze the sample at lower scale, such as SAXS and WAXS to derive a multiscale picture of the structural changes associated with deformation. Finally, the development of instrumentation for ultrafast tomographic experiments at synchrotrons[32] is recently beginning to reach a state of maturity. It could be applied to analyze deformation mechanisms in situ, thus avoiding problems related with sample relaxation.

References and Notes

(1) Meijer, H. E. H.; Govaert, L. E. Mechanical performance of polymer systems: the relation between structure and properties. *Prog. Polym. Sci.* **2005**, *30*, 915–938.

(2) Hiss, R.; Hobeika, S.; Lynn, C.; Strobl, G. Network Stretching, Slip Processes, and Fragmentation of Crystallites during Uniaxial Drawing of Polyethylene and Related Copolymers. A Comparative Study. *Macromolecules* **1999**, *32*, 4390–4403.

(3) Haward, R. N. Strain hardening of High Density Polyethylene. *J. Polym. Sci., Part B: Polym. Phys.* **2007**, *45*, 1090–1099.

(4) Bowden, P. B.; Young, R. J. Review—Deformation mechanisms in crystalline polymers. *J. Mater. Sci.* **1974**, *9*, 2034–2051.

(5) Butler, M. F.; Donald, A. M.; Brass, W.; Mant, G. R.; Derbyshire, G. E.; Ryan, A. J. A Real-Time simultaneous small- and wide-angle X-ray scattering study of In-Situ deformation of isotropic polyethylene. *Macromolecules* **1995**, *28*, 6383–6393.

(6) Butler, M. F.; Donald, A. M.; Ryan, A. J. Time resolved simultaneous small- and wide-angle X-ray scattering during polyethylene deformation—I Cold drawing of ethylene-α-olefin copolymers. *Polymer* **1997**, *38*, 5521–5538.

(7) Butler, M. F.; Donald, A. M.; Ryan, A. J. Time resolved simultaneous small- and wide-angle X-ray scattering during polyethylene deformation—II Cold drawing of linear polyethylene. *Polymer* **1998**, *39*, 39–52.

(8) Wu, W.; Wignall, G. D.; Mandelkern, L. A SANS study of the plastic deformation mechanism in polyethylene. *Polymer* **1992**, *33*, 4137–4140.

(9) Duckett, R. A. In *Plastic Deformation of Amorphous and Semi-Crystalline Materials*; Escaid, B., G'sell, C., Eds.; Les Editions de Physique: Les Ulis, France, **1982**; pp 253−264

(10) Hubert, L.; David, L.; Séguéla, R.; Vigier, G. Small-angle X-ray scattering investigation of the deformation processes in the amorphous phase of high density polyethylene. *Polym. Int.* **2004**, *53*, 582–585.

(11) Schrauwen, B. A. G.; Janssen, R. P. M.; Govaert, L. E.; Meijer, H. E. H. Intrinsic deformation behavior of semicrystalline polymers. *Macromolecules* **2004**, *37*, 6069–6078.

(12) Bartczak, Z.; Kozanecki, M. Influence of molecular parameters on high-strain deformation of polyethylene in the plane-strain compression. Part I. Stress-strain behavior. *Polymer* **2005**, *46*, 8210–8221.

(13) Kramer, E. J. Microscopic and molecular fundamentals of crazing. In *Crazing in polymers*; Kausch, H. H., Ed.; Advances in Polymer Science, 52/53; Springer: Berlin, 1983; pp 1−55.

(14) Castagnet, S.; Girault, S.; Gacougnolle, J. L.; Dang, P. Cavitation in strained polyvinylidene fluoride: mechanical and X-ray experimented studies. *Polymer* **2000**, *41*, 7523–7530.

(15) Pawlak, A.; Galeski, A. Plastic Deformation of Crystalline Polymers: The Role of Cavitation and Crystal Plasticity. *Macromolecules* **2005**, *38*, 9688–9697.

(16) Pawlak, A. Cavitation during tensile deformation of high-density polyethylene. *Polymer* **2007**, *48*, 1397–1409.

(17) Gaucher-Miri, V.; François, P.; Séguéla, R. On the mechanisms of initiation and propagation of plastic instability in polyethylene under tensile drawing. *J. Polym. Sci., B: Polym. Phys.* **1996**, *34*, 1113–1125.

(18) Wu, J. The interfacial properties and porous structures of polymer blends characterized by synchrotron small-angle X-ray scattering. *Polymer* **2003**, *44*, 8033–8040.

(19) Hay, I. L.; Keller, A. Polymer deformation in terms of spherulites. *Kolloid Z. Z. Polym.* **1965**, *204*, 43–73.

(20) Peterlin, A. Molecular model of drawing polyetyhylene and polypropylene. *J. Mater. Sci.* **1971**, *6*, 490–508.

(21) Aboulfaraj, M.; G'Sell, C.; Ulrich, B.; Dahoun, A. In situ observation of the plastic deformation of polypropylene spherulites under uniaxial tension and simple shear in the scanning electron microscope. *Polymer* **1995**, *36*, 731–742.

(22) G'sell, C.; Hiver, J. M.; Dahoun, A.; Souahi, A. Video-controlled tensile testing of polymers and metals beyond the necking point. *J. Mater. Sci.* **1992**, *27*, 5031–5039.

(23) Cazenave, J.; Seguela, R.; Sixou, B.; Germain, Y. Short-term mechanical and structural approaches for the evaluation of polyethylene stress crack resistance. *Polymer* **2006**, *47*, 3904–3914.

(24) Baravian, C.; André, S.; Renault, N.; Moumini, N.; Cunat, C. Optical techniques for in situ dynamical investigation of plastic damage. *Rheol. Acta* **2008**, *47*, 555–564.

(25) André, S., Baravian, C., Renault, N., Cunat, C. In situ mechanical characterization of polymers with the association of three optical techniques, *Appl. Phys. Lett.* **2007**, *91*, 7, 071919. DOI:10.1063/1.2768627

(26) Tang, Y.; Jiang, Z.; Men, Y.; An, L.; Enderle, H.-F.; Lilge, D.; Roth, S. V.; Gehrke, R.; Rieger, J. Uniaxial deformation of overstretched polyethylene: In-situ synchrotron small angle X-ray scattering study. *Polymer* **2007**, *48*, 5125–5132.

(27) Li, D. S.; Garmestani, H.; Alamo, R. G.; Kalidindi, S. R. The role of crystallinity in the crystallographic texture evolution of polyethylenes during tensile deformation. *Polymer* **2003**, *44*, 5355–5367.

(28) Grubb, D. T.; Prasad, K. High-Modulus Polyethylene fiber structure as shown by X-ray diffraction. *Macromolecules* **1992**, *25*, 4575–4582.

(29) Wu, J.; Schultz, J. M.; Samon, J. M.; Pangelinan, A. B.; Chuah, H. H. In situ study of structure development during continuous hot-drawing of poly(trimethylene terephthalate) fibers by simultaneous synchrotron small- and wide-angle X-ray scattering. *Polymer* **2001**, *42*, 7161–7170.

(30) Blaise, A., Baravian, C., Dillet, J., André, S. Characterization of the mesostructure of HDPE under "in-situ" uniaxial tensile test by incoherent polarized steady-light transport, *in preparation*.

(31) Hosemann, R. Crystallinity in high polymers, especially fibres. *Polymer* **1962**, *3*, 349–392.

(32) Mokso, R., Marone, F., Stampanoni, M. Real-time tomography at the Swiss Light Source. *AIP Conf. Proc.*; **2010**, in press.